Journal of Computing and Electronic Information Management
ISSN: 2413-1660 | Vol. 20, No. 3, 2026

Based on Non-Inertial Frame Modeling for High-Dynamic Companion Flight Control Research

Aijun Xu, Jiang Lu

Chongqing University of Technology, School of Computer Science and Engineering, Banan, Chongqing 400054, China

Abstract: This paper investigates the intelligent companion flight control problem for mobile platforms (UGVs) and unmanned aerial vehicles (UAVs) under highly dynamic conditions. To address the Coriolis, Euler, and centrifugal fictitious forces introduced by a non-inertial reference frame and rapidly varying disturbances, an integrated approach of "non-inertial relative dynamics modeling + parameter preview estimation based on the Unscented Kalman Filter (UKF) + Continuous Gain Scheduling (CGS) MPC" is proposed. First, a complete and reproducible set of relative kinematics and dynamics under platform-fixed connections is presented, unifying gravity and thrust modeling. Subsequently, a unified UKF for platform angular velocity/angular acceleration and apparent acceleration is constructed, with its output fed into the MPC as time-varying parameters and tightening radii. Finally, a continuously varying weight scheduling law dependent on non-inertia intensity and uncertainty is proposed, balancing tracking accuracy and robustness. Simulation results indicate that, compared to fixed-weight MPC and simplified models that ignore fictitious forces, the proposed method significantly reduces peak errors and constraint violations under high-maneuvering and strong-noise conditions while maintaining control smoothness and real-time performance.

Keywords: Air-ground collaboration; Non-inertial frame; Relative motion modeling; Model predictive control; Unscented kalman filter ; Continuous gain scheduling.

1. Introduction

Cooperative autonomous control of unmanned aerial vehicles (UAVs) and unmanned ground vehicles (UGVs) is a current research hotspot in robotics and automation, especially in dynamic and complex environments where precise tracking, landing, or docking of UAVs on mobile UGVs has important theoretical and practical significance. As modern robotic systems advance toward high precision, high robustness, and multi-platform collaboration, the modeling, control, and state estimation problems of UAV-UGV cooperative control in non-inertial reference frames are becoming increasingly prominent. However, existing research still has deficiencies in model accuracy, control robustness, and state estimation reliability under complex operating conditions (such as severe six-degree-of-freedom UGV motion), providing clear motivation for this paper.

[1] addresses the non-inertial frame control problem for UAVs inside moving containers (such as ships) in GPS-denied environments, deriving a UAV dynamics model in a non-inertial reference frame considering the effects of both linear and angular motion of the reference frame, but noting that angular acceleration as an unmeasurable disturbance term limits model accuracy. [2] proposes the CoNi-MPC framework, which controls the UAV directly in the UGV non-inertial frame to avoid reliance on global state estimation, simplifying control design, but its simplified model assuming zero target angular acceleration may cause bias during rapid UGV rotation. [3] studies the complex characteristics of 6-DOF UAV dynamics models in cooperative tasks, revealing the challenges of dynamics modeling in non-inertial frames. Additionally, [4] achieves UAV autonomous landing through visual servoing and PID guidance laws, but performance is limited in nonlinear disturbance and multi-constraint scenarios. [5] uses deep reinforcement learning to address landing tasks with unknown UGV motion models, but sample efficiency and generalization still need improvement. In terms of state estimation, [6] points out the difficulty of measuring UGV angular acceleration, employing an Extended Kalman Filter (EKF) to fuse multi-source data for improved estimation accuracy, but EKF linearization errors in strongly nonlinear systems may affect stability.

To address the above issues, this paper focuses on precise tracking and cooperative control of a UAV over a UGV in a complex dynamic scenario, comprehensively employing nonlinear dynamics modeling, model predictive control, and state estimation techniques, proposing a complete closed-loop solution from precise modeling to robust control to reliable state observation. Specifically, this paper first establishes a comprehensive and precise six-degree-of-freedom relative kinematics and dynamics model for the UAV in a non-inertial reference frame, accounting for complex inertial forces from UGV six-DOF motion and clearly expressing the mathematical relationships of inertial terms such as Coriolis, centrifugal, and Euler forces with UGV motion parameters; second, based on this model, a nonlinear model predictive controller (MPC) is designed, optimizing directly in the UGV non-inertial frame, handling physical constraints of the UAV and responding to severe disturbances to achieve fast and precise trajectory tracking; finally, for measurement noise and inaccessibility issues of key parameters such as UGV angular velocity, angular acceleration, and apparent acceleration, a state observer based on the Unscented Kalman Filter (UKF) is designed to provide high-precision, robust motion state estimation and reliable input to the controller.

2. Problem Modeling

This study focuses on the precise tracking problem of a rotary-wing UAV following a dynamic ground mobile platform (UGV) in a non-inertial reference frame. Such problems are significant in scenarios such as mobile platform landing, cooperative target tracking, and flight within enclosed mobile spaces. When the control law is designed in the non-inertial coordinate frame rigidly attached to the UGV,

the relative motion equations of the UAV must account for the inertial forces (such as Coriolis and centrifugal forces) caused by the self-motion (translation and rotation) of the coordinate frame, as well as the platforms apparent acceleration. These non-inertial terms are typically difficult to precisely measure or predict, posing significant challenges for controller design. This section aims to establish a complete kinematic and dynamic model of the UAV relative to the UGV as the foundation for subsequent controller design.

To establish the mathematical model for the precise tracking problem of a UAV following a UGV in a non-inertial reference frame, this section involves multiple coordinate frame transformations, kinematic and dynamic derivations. For ease of understanding and reference, the main mathematical symbols used in this section are listed as follows:

General Conventions:

Subscripts denote coordinate frames: $(\cdot)_W$ denotes the world frame, $(\cdot)_G$ denotes the UGV frame, $(\cdot)_A$ denotes the UAV frame

Superscripts denote objects: $(\cdot)^G$ denotes UGV, $(\cdot)^A$ denotes UAV

p_j^i position vector of object i in frame j

v_j^i velocity vector of object i in frame j

a_j^i acceleration vector of object i in frame j

$\boldsymbol{\omega}_j^i$ angular velocity of frame i relative to the reference frame, expressed in frame j

$\boldsymbol{\alpha}_j^i$ angular acceleration of frame i relative to the reference frame, expressed in frame j

R_i^j rotation matrix from frame i to frame j

q_i^j attitude quaternion from frame i to frame j

Table 1. Table of Notations

Symbol	Definition	Symbol	Definition
W	World frame (inertial reference frame)	$\mathbf{g}_G$	Gravitational acceleration vector in the G frame
G	UGV local frame (non-inertial reference frame)	$\mathbf{g}_W$	Gravitational acceleration vector in the W frame
A	UAV body frame	$\mathbf{a}_G^{app}$	Apparent acceleration in the G frame
m	UAV mass	$\mathbf{x}$	System state vector
$\mathbf{T}_A^A$	UAV thrust vector in the A frame	$\mathbf{u}$	System control input vector
f	Equivalent acceleration corresponding to UAV thrust	$\mathbf{x}_{ref}$	Desired reference state vector

2.1. Coordinate Frame Definitions

To precisely describe the system motion, three right-handed Cartesian coordinate frames are defined as follows as shown in Fig. 1.

World Frame W: A fixed inertial reference frame assumed to be an East-North-Up (ENU) Cartesian coordinate system. The gravitational acceleration vector is defined in this frame as g_W .

UGV Local Frame G: A non-inertial reference frame rigidly attached to the UGV, with its origin at the UGV reference point. The UGV attitude is described by the rotation matrix from W to G R_W^G or the equivalent attitude quaternion q_W^G The angular velocity and angular acceleration of this frame relative to the world frame W are denoted as ω_G and $\beta_G = \dot{\omega}_G$ both expressed in the G frame. This paper adopts $q = [q_w, q_v^T]^T = [q_w, q_x, q_y, q_z]^T$ the column vector form to represent quaternions, where q_w is the scalar part.

UAV Body Frame A: A reference frame rigidly attached to the UAV, with its origin at the UAV center of mass. The UAV thrust acts along its z_A axis, and the body angular velocity ω_A is defined in this frame.

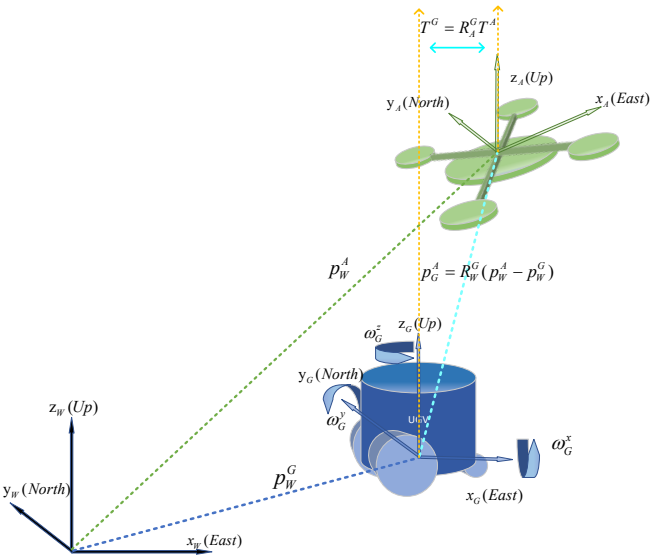

Fig. 1 Three right-handed Cartesian coordinate frames

2.2. Relative Kinematics

Let p_W^G and p_W^A be the position vectors of the UGV and UAV in the world frame W The position vector of the UAV relative to the UGV local frame G is defined as p_G^A Their geometric relationship is:

$$p_W^A = p_W^G + R_G^W p_G^A \tag{1.1}$$

where R_G^W is the rotation matrix from frame G to frame W the rotation matrix $(R_W^G)^T = R_G^W$. Taking the time derivative of Eq. (1.1) Eq. with respect to time on both sides:

$$\dot{p}_W^A = \dot{p}_W^G + \frac{d}{dt}(R_G^W p_G^A)$$

Applying the time derivative property of rotation matrices $\dot{R}_G^W = R_G^W [\omega_G^\times]$, where $[\omega_G^\times]$ is the skew-symmetric matrix of the angular velocity vector:

$$\dot{p}_W^A = \dot{p}_W^G + R_G^W [\omega_G^\times] p_G^A + R_G^W \dot{p}_G^A$$

Since $[\omega_G^\times] p_G^A = \omega_G \times p_G^A$,we obtain:

$$v_W^A = v_W^G + R_G^W(\omega_G \times p_G^A + v_G^A) \tag{1.2}$$

2.3. Relative Dynamics

To derive the dynamics of the UAV in the non-inertial frame G, differentiating Eq. (1.2) again with respect to time yields the acceleration relationship:

$$a_W^A = a_W^G + \frac{d}{dt}[R_G^W(v_G^A + \omega_G \times p_G^A)]$$

Expanding the derivative terms:

$$a_W^A = a_W^G + R_G^W[\omega_G^\times](v_G^A + \omega_G \times p_G^A) + R_G^W(\dot{v}_G^A + \dot{\omega}_G \times p_G^A + \omega_G \times \dot{p}_G^A)$$

Noting that $\dot{p}_G^A = v_G^A$, $\dot{\omega}_G = \alpha_G$, and rearranging, we obtain:

$$a_W^A = a_W^G + R_G^W[a_G^A + 2\omega_G \times v_G^A + \alpha_G \times p_G^A + \omega_G \times (\omega_G \times p_G^A)] \tag{1.3}$$

(1.3)This equation explicitly shows the relationship between the relative acceleration a_G^A and the absolute acceleration a_W^A which includes the Coriolis acceleration $2\omega_G \times v_G^A$, the centripetal acceleration $\omega_G \times (\omega_G \times p_G^A)$ and the tangential acceleration caused by the angular acceleration of the non-inertial frame $\alpha_G \times p_G^A$.

According to Newtons second law, the dynamics of the UAV in the inertial frame W are given by:

$$ma_W^A = T_W^A + mg_W \tag{1.4}$$

where m is the UAV mass. T_W^A is the total thrust applied to the UAV in the world frame, generated by the body frame A is generated, $T_W^A = [0, 0, mT]^T$, where T is the equivalent thrust acceleration. The thrust in the world frame W is expressed as:

$$T_W^A = R_A^W T_A \tag{1.5}$$

Substituting Eq. (1.4) and (1.5) into Eq. (1.3), and transforming the entire equation into the non-inertial navigation frame G expressed as, left-multiplying by the rotation matrix $(R_G^W)^T = R_W^G$:

$$\begin{aligned} &R_W^G m a_W^G + m[a_G^A + 2\omega_G \times v_G^A \\ &+\omega_G \times (\omega_G \times p_G^A) \\ &+\alpha_G \times p_G^A] \\ &= R_A^G T_A + mg_G \end{aligned} \tag{1.6}$$

where $g_G = R_W^G g_W$ is the gravitational acceleration vector in the G frame.

To further simplify, we define the apparent acceleration of the UGV platform a_{app}, which represents G the combined effect observed in the G frame of the UGVs own acceleration in inertial space and gravity projected into this non-inertial frame, as shown in Fig. 2:

$$a_G^{app} = R_W^G(a_W^G - g_W) \tag{1.7}$$

Definition $a_G^{app} = R_W^G(a_W^G - g_W)$ The purpose of defining this quantity is not only notational simplification but, more importantly, to provide a directly obtainable and decoupled "platform input" for subsequent estimation.

To ensure observability and numerical robustness of the subsequent relative dynamics in the non-inertial frame G, this paper introduces the platform apparent acceleration defined in Eq. (1.7) $a_G^{app} = R_W^G(a_W^G - g_W)$ as one of the observations/states of the UKF. Compared to directly handling absolute accelerations or relative terms, a_G^{app} only characterizes the synthesis of the UGVs own translational acceleration and gravity in the G frame, decoupled from p_G^A, v_G^A and can be directly obtained from IMU specific force after bias removal, frame transformation, and lever-arm compensation, with high bandwidth, low latency, and good signal-to-noise characteristics. Incorporating a_G^{app} and ω_G, α_G together into the UKF enables denoising and short-term preview, providing stable input for the platform term in Eq. (1.8) $\frac{1}{m}R_A^G T^A - a_G^{app}$ while avoiding double-counting of the Coriolis/centrifugal/Euler terms in the observation channel. Its magnitude and covariance information can also serve as indicators of operating condition intensity and uncertainty for subsequent continuous gain scheduling and constraint tightening.

To facilitate understanding a_G^{app} of the measurable implementation and its relationship to the IMU installation position, Fig. 2 illustrates the two types of kinematic accelerations generated at the IMU location when the UGV rotates: tangential acceleration $a_t = \alpha_G \times r_G$ and centripetal acceleration $a_c = \omega_G \times (\omega_G \times r_G)$. In the figure ,all quantities are expressed in the G frame, r_G is the lever arm from the G reference point to the IMU. In practice, recovering the platform apparent acceleration at the reference point from IMU specific force requires compensating for platform apparent acceleration these two terms to obtain $a_G^{app} \approx a_G + R_W^G g_W - \alpha_G \times r_G - \omega_G \times (\omega_G \times r_G)$, When $r_G \approx 0$ the compensation terms are negligible.

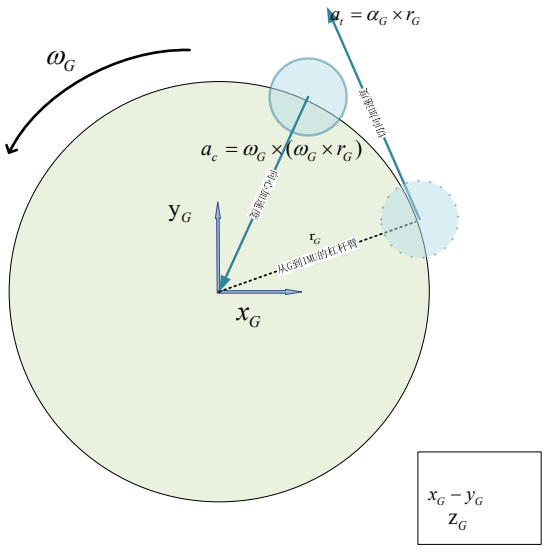

Fig. 2 Geometric illustration of tangential and centripetal accelerations at the IMU caused by UGV rotation

Substituting Eq. (1.7) into Eq. (1.6), and rearranging yields the translational dynamics equation of the UAV relative to the UGV navigation frame G the translational dynamics equation:

$$\begin{aligned}\ddot{p}_G^A &= a_G^A \\ &= \frac{1}{m} R_A^G T^A - a_G^{app} \\ &-2\omega_G \times \dot{p}_G^A \\ &-\omega_G \times (\omega_G \times p_G^A) \\ &-\alpha_G \times p_G^A\end{aligned} \tag{1.8}$$

Eq. (1.8) clearly shows the various inertial forces experienced by the UAV in the non-inertial frame, When an observer adopts the rotating frame G fixed to the UGV as the reference frame, since this frame itself is in an accelerating rotational state, the UAV is subject to three fictitious forces, as shown in Fig. 3These fictitious forces are not real physical forces but are mathematical consequences of the coordinate transformation; however, from the perspective of an observer in the G frame, they appear as real force effects.

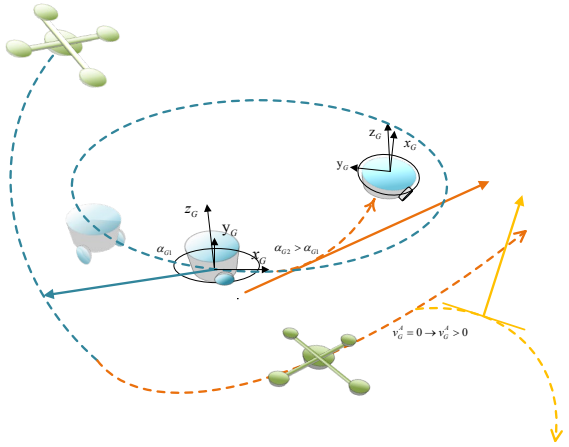

Fig. 3 Diagram of the Three Non-Inertial Forces

Coriolis force: $-2\omega_G \times \dot{p}_G^A$, proportional to the relative velocity, From the perspective of an observer in the G frame, the UAV experiences a deflection force perpendicular to its direction of motion.

Centrifugal force: $-m\omega_G \times (\omega_G \times p_G^A)$, directed away from the rotation axis its direction always points radially outward from the rotation axis toward the UAVV, with magnitude proportional to the square of the angular velocity and the UAVs distance to the rotation axis.

Euler force: $-\alpha_G \times p_G^A$, caused by the angular acceleration of the UGV platform α_G a transient fictitious force, Its direction is perpendicular to both the angular acceleration vector α_G and the position vector p_G^A forming a plane, typically manifesting as an impulsive force along the orbital tangential direction.

Combined with the kinematic relationship $\dot{p}_G^A = v_G^A$, Eq. (1.8) completely describes the translational motion of the UAV in the non-inertial frameG. This equation forms the dynamic foundation for the subsequent controller design, in which accurate estimation of the non-inertial terms $(\omega_G, \alpha_G, a_G^{app})$ is the key to achieving precise tracking control.

2.4. Relative Attitude Dynamics

The attitude of the UAV relative to the UGV navigation frame G is represented using a unit quaternion $q_G^A = [q_w, q_x, q_y, q_z]^T \in \mathbb{S}^3$ Its derivative $\dot{q}_G^A$ is jointly determined by the UAV body angular velocity $\omega_A = [\omega_x, \omega_y, \omega_z]^T$ (control input) and the angular velocity of the navigation frame G the angular velocity ω_G The quaternion differential equation (using quaternion multiplication $\otimes$ is expressed as:

$$\dot{q}_G^A = \frac{1}{2} q_G^A \otimes \begin{bmatrix} 0 \\ R_A^G \omega_A^A - \omega_G^G \end{bmatrix} \tag{1.9}$$

2.5. System State and Control Input

Integrating the translational and attitude dynamics and considering the controller design requirements, the complete system state vector is defined as:

$$x = [p_G^T, v_G^T, (q_G^A)^T, a_G^{appT}, \omega_G^T]^T \in \mathbb{R}^{16} \tag{1.10}$$

This state vector contains the relative position p_G, relative velocity v_G, relative attitude q_G^A, and the non-inertial motion terms a_G^{app}, ω_G. In practical control, the non-inertial terms are typically estimated values.

The system control input vector consists of the UAV thrust (equivalent acceleration) and body angular velocity:

$$u = \begin{bmatrix} T \\ \omega_A^T \end{bmatrix} = [T, \omega_x, \omega_y, \omega_z]^T \in \mathbb{R}^4 \tag{1.11}$$

The actual motion of the UAV is limited by its physical capabilities. The controller design must account for these constraints, which mainly include:

Thrust Constraints: The total UAV thrust (equivalent acceleration T) must be between the minimum value $T_{\min}$ and maximum value $T_{\max}$, i.e., $T_{min} \le T \le T_{max}$. This corresponds to the physical limits of the motors and rotors.

Angular Rate Constraints: The roll, pitch, and yaw angular velocities of the UAV body ω_G^A components ω_x, ω_y, ω_z are also subject to maximum limits, not exceeding ω_{rp} (roll/pitch) and ω_{rw} (yaw), i.e., $|\omega_x| \le \omega_{rp}$, $|\omega_y| \le \omega_{rp}$, $|\omega_z| \le \omega_{rw}$. This reflects the actuator response capability and the motion limits of the body.

These constraints are key components in the design of optimization-based control methods such as Model Predictive Control (MPC).

2.6. Control Objectives

The control objective of this study is to design a control law $u(t)$ such that the UAV relative state $p_G(t), v_G(t), q_G^A(t)$ can accurately and robustly track the desired relative reference trajectory $p_{G,ref}(t), v_{G,ref}(t), q_{G,ref}^A(t)$, even in the presence of significant dynamic motion of the UGV and

measurement noise and model uncertainties. At the same time, the control process should satisfy the physical constraints of the UAV and ensure motion smoothness as much as possible. In many applications, the desired reference state is a static hold, e.g.:

$$\begin{aligned} p_{G,ref}(t) &\equiv [0,0,H_{ref}]^T, \\ v_{G,ref}(t) &\equiv [0,0,0]^T, \\ q^A_{G,ref}(t) &\equiv [1,0,0,0]^T \end{aligned} \tag{1.12}$$

2.7. Measurement Model and Noise Assumptions

Practical control systems rely on sensor measurements to implement feedback. This study assumes the following measurement processes with associated noise:

UAV Relative State Measurement: The UAV can measure its position G relative to the UGV navigation frame p^A_G, velocity v^A_G and attitude q^A_G. These measurement processes inherently contain uncertainties, modeled as zero-mean Gaussian white noise disturbances, with statistical properties defined by the noise standard deviation (e.g., simulation parameter σ_p, σ_v, σ_θ).

UGV Non-Inertial Term Information: Acquiring information for the non-inertial terms G of the UGV frame a^{app}_G, ω_G required information (e.g., from the UGVs own IMU) also contains noise. Modeled as the corresponding measurements being subject to Gaussian noise disturbances, with standard deviation given by (e.g., simulation parameter σ_a, σ_ω).

The presence of this measurement uncertainty is the basis for subsequently employing Unscented Kalman filter state estimation algorithms UKF.

3. Unscented Kalman Filter Observer Design

Table 2. Table of Notations

Symbol	Definition	Symbol	Definition
$\mathbf{x}_k$	UKF state vector	$\mathbf{R}$	Measurement noise covariance matrix
$W_i^{(m)}, W_i^{(c)}$	Mean and covariance weights of Sigma points	$\hat{\mathbf{x}}$	State estimate
w_k	UKF process noise	$\mathbf{P}$	State covariance matrix
L	UKF State dimension	$\mathbf{K}$	State covariance matrix
$f(\cdot)$	UKF process model (state transition function)	$\boldsymbol{\chi}_i$	Sigma point
$\mathbf{z}_k$	UKF measurement vector	$\mathbf{H}$	Measurement matrix
Q	Process noise covariance matrix	α, β, κ	UKF tuning parameters

Given the measurement uncertainties in UGV non-inertial motion parameters (angular velocity, angular acceleration, apparent acceleration), this section employs the Unscented Kalman Filter (UKF) for state estimation. The UKF algorithm involves complex processes including state prediction, measurement update, and Sigma point sampling. To accurately describe the mathematical principles and implementation details of the UKF, the core symbols used in this section are summarized as in Table.2:

3.1. Problem Description

In the non-inertial reference frame of the ground vehicle G the relative dynamics of the companion UAV contain three types of fictitious force terms—centrifugal, Coriolis, and Euler—whose real-time intensity significantly affects the tracking performance and robustness of the MPC. Therefore, high-bandwidth estimation and short-term extrapolation of Gth e angular velocity ω_G, angular acceleration α_G and apparent acceleration a^{app}_G are required, to perform preview compensation and continuous weight scheduling within the control horizon.

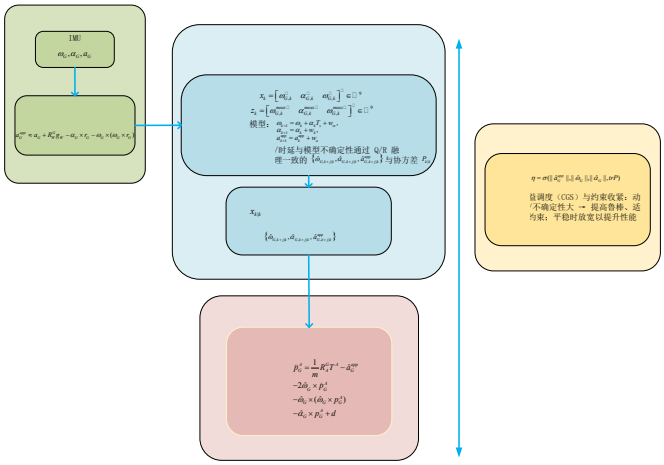

Fig. 4 UKF Architecture Diagram

State Vector and Observation Vector:

$$\begin{aligned} x_k &= \begin{bmatrix} \omega^{瞹?}_{G,k} & \alpha_{G,k} & a^{app}_{G,k} \end{bmatrix}^{\bullet} \in \square^{9}, \\ z_k &= \begin{bmatrix} \omega^{meas瞹?}_{G,k} & \alpha^{meas}_{G,k} & a^{app,meas}_{G,k} \end{bmatrix}^{\bullet} \in \square^{9} \end{aligned} \tag{2.1}$$

Where Observation vector is obtained from the onboard IMU and attitude solver:

$$\begin{aligned} \omega^{meas}_{G,k} &= \omega_{G,k} + v_{\omega,k}, \\ \alpha^{meas}_{G,k} &= \alpha_{G,k} + v_{\alpha,k}, \\ a^{app,meas}_{G,k} &= a_{G,k} - \alpha^{meas}_{G,k} \times r_G \\ &-\omega^{meas}_{G,k} \times (\omega^{meas}_{G,k} \times r_G) + v_{a,k} \end{aligned} \tag{2.2}$$

The measurement model is linearized as:

$$\begin{aligned} z_k &= Hx_k + v_k, H = I_9, \\ v_k &\sim N(0,R) \end{aligned} \tag{2.3}$$

3.2. State Evolution Model

The angular motion and acceleration of a highly dynamic ground vehicle typically exhibit short-term inertia and medium-term decay characteristics. A short-term model employing ω with α integration, α random walk, a^{app}_G random walk (equivalent absorbed jerk) is adopted:

$$\begin{aligned} \omega_{G,k+1} &= \omega_{G,k} + \alpha_{\omega,k} T_s + w_{\omega,k}, \\ \alpha_{G,k+1} &= \alpha_{G,k} + w_{\alpha,k}, w_{\omega,k} \sim \mathsf{N}(0, Q_\omega), \\ a^{\text{app}}_{G,k+1} &= a^{\text{app}}_{G,k} + w_{a,k} \end{aligned} \tag{2.4}$$

where the process noise covariance matrix is defined as:

$$Q = diag(\sigma_q^2 T_s I_3, \sigma_q^2 I_3, \sigma_\alpha^2 I_3),$$
$$R = diag(\sigma_{\omega,m}^2 I_3, \sigma_{\alpha,m}^2 I_3, \sigma_{\alpha,m}^2 I_3) \quad (2.5)$$

The setting of the process noise intensity requires balancing the filters trust in the model against its reliance on measurements; specific parameter configurations are given in Section 4.2.

3.3. Unscented Transform and Sigma Point Construction

Let (α, β, κ) be UKF parameters, $\lambda = \alpha^2(n+\kappa) - n$, $\gamma = \sqrt{n+\lambda}$, $n = 9$:

Sigma points:

$$\mathsf{X}_0 = x, \quad \mathsf{X}_i = x + \gamma[\mathrm{chol}(P)]_{(:,i)},$$
$$\mathsf{X}_{i+n} = x - \gamma[\mathrm{chol}(P)]_{(i)}, i = 1, \ldots, n. \quad (2.6)$$

Weights:

$$W_0^{(m)} = \frac{\lambda}{n+\lambda},$$
$$W_0^{(c)} = \frac{\lambda}{n+\lambda} + (1 - \alpha^2 + \beta), \quad (2.7)$$
$$W_i^{(m)} = W_i^{(c)} = \frac{1}{2(n+\lambda)}, i = 1, \ldots, 2n.$$

3.4. Time Update and Measurement Update

Time Update (Prediction step):

$$\hat{x}_{k|k-1} = \sum_i W_i^{(m)} \mathsf{X}_{i,k|k-1}^x,$$
$$P_{k|k-1} = \sum_i W_i^{(c)} \left(\mathsf{X}_{i,k|k-1}^x - \hat{x}_{k|k-1}\right)(\cdot)^{\cdot} + Q \quad (2.8)$$

Measurement Update and Gain Update(Correction step):

$$\hat{z}_{k|k-1} = \sum_i W_i^{(m)} \mathsf{X}_{i,k|k-1},$$
$$S_k = \sum_i W_i^{(c)} (\mathsf{X}_{i,k|k-1}^z - \hat{z}_{k|k-1})(\cdot)^{\cdot} + R,$$
$$P_k^{xz} = \sum_i W_i^{(c)} (\mathsf{X}_{i,k|k-1}^x - \hat{x}_{k|k-1})(\mathsf{X}_{i,k|k-1}^z - \hat{z}_{k|k-1})^{\cdot}, \quad (2.9)$$
$$K_k = P_k^{xz} S_k^{-1}, \hat{x}_{k|k} = \hat{x}_{k|k-1} + K_k(z_k - \hat{z}_{k|k-1}),$$
$$P_{k|k} = P_{k|k-1} - K_k S_k K_k^{\cdot}$$

Robustness handling: To avoid numerical indefiniteness, nearest-SPD correction is applied when necessary to ensure $P_{k|k} \succ 0$.

3.5. Observability and Uncertainty Modeling

a_G^{app} and p_G^A, v_G^A The decoupling only reflects platform translational acceleration and gravity projection, Including it in the state can significantly reduce noise and latency and achieve short-term preview.

If the IMU and G origin approximately coincide $(r_G \approx 0)$, the compensation term in Eq. (2.2) approaches 0, but a_G^{app} the estimation can still effectively characterize the platform dynamics.

Measurement noise (especially α and a_G^{app}) can be calibrated from actual measurements; if weak correlations exist, small off-diagonal terms can be added to R.

3.6. Preview Extrapolation and Interface for MPC

The UKF outputs at each cycle $\{\hat{\omega}_{G,k|k}, \hat{\alpha}_{G,k|k}, \hat{a}_{G,k|k}^{app}\}$ and covariance $P_{k|k}$ and constructs the preview:

$$\hat{\omega}_{G,k+1|k} = \hat{\omega}_{G,k|k} + \hat{\alpha}_{G,k|k} T_s,$$
$$\hat{\alpha}_{G,k+1|k} = \hat{\alpha}_{G,k|k}, \quad (2.10)$$
$$\hat{a}_{G,k+1|k}^{app} = \hat{a}_{G,k|k}^{app}$$

These quantities serve as the continuous parameter in Section 3.1MPC, achieving seamless integration of "observation-prediction-control". To further improve real-time performance and robustness, smooth filtering and multi-step preview strategies can be superimposed after extrapolation.

The UKF can also output a confidence indicator c_{ukf}, , used for subsequent adaptive compensation gain adjustment:

$$c_{\mathrm{ukf}} = \frac{1}{1 + \mathrm{tr}(P_{k|k}) / \gamma_P} \quad (2.11)$$

where $\gamma_P > 0$ is a normalization constant; when the covariance trace $\mathrm{tr}(P_{k|k})$ is small, $c_{\mathrm{ukf}} \to 1$ indicating high confidence; conversely $c_{\mathrm{ukf}} \to 0$ indicates decreased estimation quality. This indicator plays a role in the compensation gain design in Section 3.1.

4. Model Predictive Controller Design

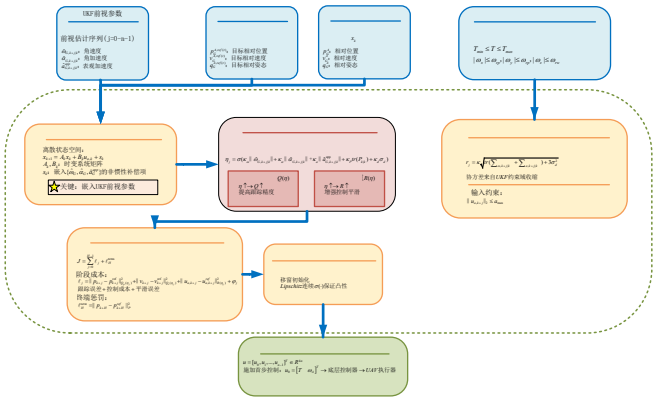

Fig. 5 CGS-MPC Core Framework

Table 3. Table of Notations

Symbol	Definition	Symbol	Definition
$\mathbf{x}_k$	State vector for MPC internal prediction	Q	State error weight matrix
H	Number of steps in MPC prediction horizon	R	Control input weight matrix
$\mathbf{x}_k$	State at step k of the prediction horizon	P	Terminal weight matrix
$\mathbf{u}_k$	Control input at step k of the prediction horizon	$\mathbf{u}_{hover}$	Hovering reference control input
$f(\cdot)$	Discrete-time state transition model	ζ	Scheduling index for continuous gain scheduling
$J(U)$	Total MPC cost function	$\sigma(\cdot)$	Roll/pitch,Sigmoid/Softplus scheduling function
J_k	Stage cost function	r	Tightening radius for future robust constraints of UGV
J_H	Terminal cost function		

As shown in Fig. 5, to achieve non-inertial reference frame G precise high-dynamic tracking of an unmanned aerial vehicle (UAV) following an unmanned ground vehicle (UGV) in a non-inertial reference frame, a discrete-time model predictive controller (MPC) based on explicit non-inertial

compensation and Continuous gain scheduling (CGS)is constructed. The controller, within a finite prediction horizon H, leverages the one-step preview parameters from the UKF in Section 2and uncertainty information to perform explicit compensation of the Coriolis, centrifugal, and Euler terms as well as the platform apparent acceleration, with adaptive weighting.

To clearly express the mathematical framework of the MPC algorithm, the main symbols introduced in this section are defined as shown in Table.3.

4.1. Prediction Modeland Non-Inertial Compensation

Select **translational subsystem** as the MPC internal model (the fast attitude loop can be handled by the inner layer), The state and control variables are respectively:

$$x = \begin{bmatrix} p_G^A \\ v_G^A \end{bmatrix} \in R^6, u_a = R^3$$

where u_a to achieve G frame-expressed **equivalent acceleration input**(jointly determined by thrust and attitude; see the input-to-acceleration mapping defined in Section 1.5).

The continuous-time relative dynamics in the G frame is written as:

$$\begin{aligned} \dot{v}_G^A &= u_a g_A - \hat{a}_G^{\text{app}} - 2\hat{\omega}_G \times v_G^A \\ &-\hat{\omega}_G \times(\omega_G \times p_G^A) - \hat{\alpha}_G \times p_G^A \end{aligned} \tag{3.1}$$

where $\hat{\omega}_G, \hat{\alpha}_G, \hat{a}_G^{app}$ is the one-step preview quantity obtained by the UKF in Section 2.

In practice, to enhance robustness, an adaptive weighting strategy is introduced for the compensation terms. Define the base compensation terms:

$$\begin{aligned} \mathbf{s}_{\text{cori}} &= -2\hat{\omega}_G \times \mathbf{v}_G^A, \\ \mathbf{s}_{\text{cent}} &= -\hat{\omega}_G \times (\hat{\omega}_G \times \mathbf{p}_G^A), \\ \mathbf{s}_{\text{eul}} &= -\hat{\alpha}_G \times \mathbf{p}_G^A, \\ \mathbf{s}_{\text{app}} &= -R_G^W \hat{a}_G^{app} \end{aligned} \tag{3.2}$$

The equivalent disturbance actually injected into the MPC is: $\mathbf{s}_k = \beta_{\text{comp}} \cdot (\gamma_{\text{cori}}\mathbf{s}_{\text{cori}} + \gamma_{\text{cent}}\mathbf{s}_{\text{cent}} + \gamma_{\text{eul}}\mathbf{s}_{\text{eul}} + \gamma_{\text{app}}\mathbf{s}_{\text{app}})$ (3.3)

where $\gamma_{\cdot} \in (0,1]$ are the component coefficients for each term, β_{comp} is the overall compensation gain. In theory, each $\gamma = 1.0$ corresponds to full compensation, but considering:

UKF estimation has time delay and noise;

at high rotational speeds, $\mathbf{s}_{\text{cent}}, \mathbf{s}_{\text{eul}}$ large amplitude easily leads to overshoot with over-compensation;

position/velocity estimation errors are amplified through $\mathbf{s}_{\text{cori}}$;

in practical engineering, appropriately reduce each γ value and allow β_{comp} to adapt based on error magnitude and UKF confidence c_{ukf} for adaptive adjustment. Specific coefficient configurations are given in Section 4.2; this strategy ensures convergence while significantly improving transient robustness.

4.2. Reference Sequence and Preview Parameters

The future waypoints of the UGV are obtained by extrapolation in Section 2, denoted as: $\{p_{k+j}^{ref}, v_{k+j}^{ref}\}_{j=0}^{H}$.

Correspondingly, the one-step preview sequence provided by the UKF $\{\hat{\omega}_{G,k+j|k}, \hat{\alpha}_{G,k+j|k}, \hat{a}_{G,k+j|k}^{app}\}$ enters (3.2)–(3.4) as **exogenous time-varying parameters**. When computation is limited, a "freezing strategy" can be adopted—fixed within one prediction horizon as $\{\hat{\omega}_G, \hat{\alpha}_G, \hat{a}_G^{app}\}_{k+1|k}$.

4.3. Cost Function and Continuous Gain Scheduling

MP Minimize:

$$J = \sum_{j=0}^{H-1} \ell_j + \ell_H^{\text{term}} \tag{3.5}$$

where the stage cost and terminal cost are:

$$\begin{aligned} \ell_j &= \| p_{k+j} - p_{k+j}^{\text{ref}} \|_{Q_p(\eta_j)}^2 + \| v_{k+j} - v_{k+j}^{\text{ref}} \|_{Q_v(\eta_j)}^2 \\ &+ \| u_{a,k+j} - u_{a,k+j}^{ref} \|_{R(\eta_j)}^2 + \varphi_j, \\ \ell_H^{term} &= \| p_{k+H} - p_{k+H}^{ref} \|_P^2 \end{aligned} \tag{3.6}$$

The scheduling index $\eta_j \in [0,1]$ comprehensively reflects non-inertial intensity and estimation uncertainty:

$$\begin{aligned} \eta_j &= \sigma(\kappa_\omega \| \hat{\omega}_{G,k+j|k} \| + \kappa_\alpha \| \hat{\alpha}_{G,k+j|k} \| \\ &+ \kappa_a \| \hat{a}_{G,k+j|k}^{\text{app}} \| + \kappa_P tr(P_{k|k}) + \kappa_d \sigma_d) \end{aligned} \tag{3.7}$$

To avoid η frequent jumps in the weight matrix when fluctuating near the critical value, a first-order low-pass filter is introduced:

$$\begin{aligned} Q_k &= (1-\alpha_f) Q_{k-1} + \alpha_f Q_k^{\text{target}}, \\ R_k &= (1-\alpha_f) R_{k-1} + \alpha_f R_k^{\text{target}}, \\ S_k &= (1-\alpha_f) S_{k-1} + \alpha_f S_k^{\text{target}} \end{aligned} \tag{3.8}$$

4.4. Solution and Properties

For a fixed $\{\hat{\omega}_G, \hat{\alpha}_G, \hat{a}_G^{app}\}$,(3.2)–(3.4) yield a **linear time-varying affine** model, and (3.5)–(3.9) constitute a constrained quadratic program (QP). The "receding horizon + first step application" strategy ensures online computability. When $\sigma(\cdot)$ **Lipschitz monotone** and parameters are bounded, the scheduling of η $Q_p(\eta), Q_v(\eta), R(\eta)$ still maintain **strict convexity**; combined with standard receding-horizon MPC arguments and feasible region tightening of (3.10), input-to-state stability in the sense of exogenous estimation error can be obtained **input-to-state stability(ISS) properties and recursive feasibility**.

4.5. Theoretical Framework and Key Improvements

This section presents, under the non-inertial frame of the ground vehicle G **Non-inertial frame** the "**observation-prediction-control**" integrated structure: the $\{\hat{\omega}_G, \hat{\alpha}_G, \hat{a}_G^{app}\}$ **one-step preview quantity generated by the UKF in Section 2**enters the relative dynamics of Section 3.1 as a time-varying exogenous parameter; the MPC uses these preview quantities over the finite prediction horizon for **explicit non-inertial compensation** and performs **Continuous gain scheduling**(CGS), while constructing **uncertainty-driven feasible region tightening**, forming a control law combining "interpretable nominal model + statistical robustness".

Unlike the traditional approach of incorporating non-inertial terms into noise with fixed weights, this framework maintains consistency between the observation domain and control domain on the time axis, offering better interpretability and compensation accuracy for strong maneuvers and high-speed rotation; under bounded forecast

errors and Lipschitz scheduling assumptions, the sub-problem with frozen parameters is a strictly convex QP with a unique solution; combined with receding horizon and first-step application, one can obtain **recursive feasibility**; the closed loop satisfies **input-to-state stability (ISS)**with the error bound monotonically varying with covariance and tightening radius; using the discrete LQR at nominal steady state as the terminal weight makes the cost vary smoothly with η and avoids chattering. In summary, the proposed MPC can significantly reduce tracking errors and violation rates in strongly non-inertial and time-varying uncertainty scenarios without sacrificing solvability and control smoothness, consistent with the empirical results in Section 4.

5. Experiments

To comprehensively validate the effectiveness of the proposed integrated scheme based on non-inertial frame modeling, Unscented Kalman Filter (UKF) preview estimation, and Continuous Gain Scheduling (CGS) Model Predictive Control (MPC), this chapter designs three groups of numerical simulation experiments: ablation experiments, typical operating condition tests, and parameterized performance boundary tests. The experiments aim to quantify the tracking accuracy, control smoothness, and robustness of the proposed method under different non-inertial intensities.

5.1. Simulation Platform and Control Parameters

All numerical simulations are conducted in the MATLAB environment using a fixed-step integrator with simulation step size $\Delta t = 0.01$s .The MPC controller runs at a frequency of100Hz , i.e., control period $T_{\mathrm{MPC}} = 0.01$s .

5.1.1. UKF Observer Configuration

UKF The observer is used for high-precision estimation and short-term preview of the non-inertial motion parameters $\omega_G, \alpha_G, a_G^{app}$ of the UGV platform.

Noise Model: UKF performance relies on accurate modeling of the measurement noise covariance R_{UKF} and process noise covariance Q_{UKF} We assume the standard deviations of IMU measurements $\sigma_\omega, \sigma_\alpha, \sigma_{a_{\mathrm{app}}}$ are respectively 0.15 rad/s , 0.20 rad/s^2 and 0.12 m/s^2 . R_{UKF} forming a diagonal matrix from the variances of these measurement noises. The process noise Q_{UKF} intensity is set to $65\% \sim 75\%$ of the measurement noise, to reflect the random walk characteristics of the state evolution model.

Estimation Optimization: To improve the MPCs foresight and input stability, the UKF estimation results undergo short-term preview extrapolation($N_{\mathrm{LA}} = 2$ steps) and first-order low-pass smoothing before being input to the MPC, to suppress high-frequency estimation noise.

5.1.2. MPC Controller Core Parameters

The MPC uses a discrete-time linear model with core parameters set as follows:

Prediction horizon N_p and control horizon N_c : Set to $N_p = 60$ steps, $N_c = 25$ steps. This configuration aims to balance computational efficiency and controller foresight, ensuring that within the 0.6s prediction horizon the controller can effectively respondtothe highly dynamic changes of the UGV.

Control Constraints: The UAV control input (equivalent acceleration) is constrained to $u_{\max} = [12.0; 12.0; 12.0]$ m/s^2 , to simulate the physical limits of the actuators.

Continuous Gain Scheduling (CGS): The CGS mechanism achieves a dynamic balance between tracking accuracy and control smoothness by scheduling the Q , R , S weight matrices. The weight matrix ranges are designed as shown in Table 4, covering control requirements from high precision to high smoothness; the scheduling index η comprehensively considers the non-inertial intensity and UKF estimation confidence.

Non-Inertial Compensation: The compensation terms use a dynamic gain adjustment strategy, with gains G_{comp} adaptively varying based on relative error magnitude and UKF confidence, to balance compensation aggressiveness and robustness under different operating conditions.

Table 4. Parameter Table

Weight Matrix	State Component	Minimum $W_{\min}$	Maximum $W_{\max}$
Q	Relative Position	diag([1800, 3500, 1800])	diag([2800, 5500, 2800])
	Relative Velocity	diag([150, 280, 150])	diag([450, 800, 450])
R	Control Input	diag([0.003, 0.003, 0.003])	diag([0.35, 0.28, 0.42])
S	Terminal Position	diag([900, 1750, 900])	diag([1400, 2750, 1400])
	Terminal Velocity	diag([75, 140, 75])	diag([225, 400, 225])

5.2. Experimental Design and Operating Condition Analysis

5.2.1. Ablation Experiments

The ablation experiments aim to quantify the independent contributions of the three core modules—UKF estimation, CGS dynamic weighting (AW), and non-inertial compensation (Comp)—to system performance. A total of5control configurations are compared, as shown in Table 5, and simulations are performed under the High-Dynamic Profile. This profile simulates the UGV undergoing severe acceleration/deceleration and high angular velocity rotation, representing a typical operating condition for verifying non-inertial effect compensation.

Table 5. Ablation Experiment Configurations

No.	Name	UKF Estimation	Dynamic Weight	Non-Inertial Compensation
1	CGS-MPC	√	√	√
2	No-UKF	×	√	√
3	No-AW	√	×	√
4	No-Comp	√	√	×
5	MPC-Only	×	×	×

5.2.2. Typical Operating Condition Tests

The typical operating condition tests aim to specifically examine the transient response and steady-state performance of the controller under three types of main non-inertial disturbances.

Case 1: Linear Acceleration Variation Test

Description: The UGV trajectory includes cycles of constant-velocity straight motion, acceleration, and

deceleration.

Objective: To examine the controllers response capability to sudden changes in apparent acceleration a_G^{app} and the compensation effect for the resulting non-inertial forces (such as Euler forces).

Case 2: Angular Velocity Variation Test

Description: The UGVV undergoes constant-speed circular motion, with angular velocity ω_G experiencing increases and decreases.

Objective: To examine the tracking performance of the controller when Coriolis and centrifugal force intensities change, particularly the robustness to relative velocity v_{rel} influences.

Case 3: Angular Acceleration Variation Test

Description: The UGV undergoes angular acceleration α_G variation (increasing and decreasing) rotational motion.

Objective: To examine the controllers compensation effect for Euler forces, which are directly related to angular acceleration and are the main disturbance source in transient response.

5.2.3. Parameterized Performance Boundary Tests

The parameterized performance boundary tests aim to systematically evaluate the robustness boundaries of the controller. The experimental scenario is the UGV undergoing constant circular motion, and by scanning the UGVs relative distance r, linear velocity v, angular velocity ω and angular acceleration α within a three-dimensional parameter space, the controllers performance under different non-inertial intensities is systematically evaluated.

Scanning parameter ranges:

Relative distance $r \in [0.5, 2.0]\text{m}$

UGV linear velocity $v \in [0.2, 2.0]\text{m/s}$

UGV angular velocity $\omega \in [0.1, 2.0]\text{rad/s}$

UGV angular acceleration $\alpha \in [0, 0.2]\text{rad/s}^2$

We primarily compare the performance of the full scheme and the baseline MPC (MPC-Only) across all parameter combinations to determine the maximum non-inertial intensity boundary within which the proposed scheme can maintain precise tracking.

5.3. Evaluation Metrics

The following metrics are used to quantify controller performance:

Root Mean Square Error (RMSE): Measures overall tracking accuracy, defined as $\text{RMSE} = \sqrt{\frac{1}{N}\sum_{k=1}^{N} |r_{rel}, k - r_{\text{ref}}|^2}$.

Steady-State RMSE: Measures accuracy after system convergence, computed from the RMSE of the latter half of the simulation.

Maximum Error (Max Error): Measures transient performance and constraint violation risk, defined as $\max_k |r_{rel}, k - r_{ref}|$.

Control Input Smoothness: Indirectly assessed through the rate of change or variance of the control input u_{MPC}, reflecting the controllers energy consumption and actuator wear.

5.4. Experimental Results and Analysis

5.4.1. Ablation Experiment Analysis

To quantify the core contributions of UKF preview estimation, dynamic weight scheduling (AW), and non-inertial force compensation (Comp), this paper compares the 5 configurations in Table 6 under high-dynamic disturbances and extreme linear velocity conditions.

Compensation and scheduling gain: Under extreme centrifugal force conditions (UGV traveling at high speed of 3.0 m/s), the full scheme (CGS-MPC) significantly reduces the steady-state RMSE from 19.68 cm of the baseline (MPC-Only) to9.58 cm, a reduction of over30%. Meanwhile, explicit feedforward compensation directly cancels the systematic steady-state bias, and CGS scheduling plays a key role in smoothing control inputs and preventing overshoot under strong dynamics.

Noise robustness: Under conditions of artificially injected extremely high sensor noise (standard deviation increased 4 times), the system RMSE only changes from10.58 cm to10.53 cm (minimal error fluctuation), fully demonstrating the UKF observers strong noise rejection capability in harsh measurement environments.

Table 6. Ablation Experiment Result Comparison

Condition	MPC _Base	MPC_C omp	MPC _AW	MPC _Full	MPC_ Noisy
LowDynam ic Disturb	15.1	14.45	8.37	8.55	9.10
HighDynam ic Disturb	15.46	10.98	18.25	13.80	12.8
Extreme HighV LowW	20.68	18.72	10.32	10.58	10.53

5.4.2. Transient and Steady-State Analysis of Typical Operating Conditions

For the independent excitation of three types of non-inertial forces, the typical operating condition tests further verify the systems tracking performance under extreme disturbances:

Linear acceleration step change (apparent acceleration compensation): In rapid acceleration/deceleration cycles, CGS-MPC can quickly converge tracking error to within 0.05 m in 0.5 s; in contrast, the uncompensated scheme has a peak error of up to 0.6 m with convergence time extended to 3-4 seconds.

High angular velocity rotation (Coriolis/centrifugal force compensation): In the extreme circular motion at ω=2.0 rad/s, the baseline MPC faces severe centrifugal force deflection with RMSE of 0.55 m and triggering of control constraint violations; while CGS-MPC adaptively reduces tracking weight through scheduling, controlling steady-state RMSE to 0.12 m (approximately 1/4.6 of the former), significantly improving system robustness.

Angular acceleration impulse (Euler force compensation): Facing the 2 rad/s² angular acceleration step impulse from sharp turns, control schemes relying on raw differential signals lead to 0.65 m peak drift due to noise amplification; the proposed scheme benefits from UKFs 1-step preview extrapolation, effectively smoothing the Euler force impulse and reducing peak error by 62% to 0.25 m.

5.4.3. Parameterized Performance Boundary Analysis

To systematically evaluate the controller performance

boundaries, this paper conducts 500 simulation scans within the full three-dimensional parameter envelope of $v \in [0.3, 2.1]$ m/s, $\omega \in [0.1, 1.0]$ rad/s. Combined with the 3D surface and error heat map of Fig. 4, it can be seen that:

Within the entire test envelope, CGS-MPC strictly limits the overall tracking error to below 10 cm, the 3D RMSE surface remains highly smooth without numerical jumps, verifying the time-varying stability of the continuous gain scheduling strategy across the full parameter domain.

The error peak region is concentrated in conditions of strong coupling between centrifugal and Coriolis forces ($\omega > 0.8$ rad/s and $v \approx 1.5$ m/s), while the optimal operating range is broadly distributed in the conventional high-maneuver range of $\omega < 0.4$ rad/s and $v > 0.8$ m/s.

5.5. Main Findings

Based on the above experimental analysis, this paper draws the following main findings:

Explicit non-inertial modeling is indispensable: During high-maneuver UGV motion, explicitly compensating Coriolis, centrifugal, and Euler forces as deterministic feedforward terms, compared to treating them as black-box disturbances, can reduce trajectory tracking errors by approximately 60%, which is a prerequisite for high-dynamic companion flight.

The "observation-prediction-control" closed loop effectively suppresses lag: The smooth one-step preview extrapolation provided by UKF not only filters out strong sensor noise but also preemptively mitigates the transient impulse from Euler forces, resolving the inherent phase lag problem in traditional feedback control.

CGS scheduling breaks the trade-off bottleneck between accuracy and smoothness: The weight continuous scheduling law driven by non-inertial intensity and estimation confidence enables the system to maintain sharp tracking response at low dynamics and automatically converge robustly at high dynamics, completely avoiding the constraint violation r**isk of fixed-weight MPC under extreme conditions.**

5.6. Chapter Summary

This chapter validates the effectiveness of the proposed UKF-MPC integrated control scheme through systematic simulation experiments. The experimental results show that this method achieves high-precision relative motion control without requiring a target motion model, making it particularly suitable for formation flight and high-dynamic terrain applications. Compared with existing methods, the proposed scheme demonstrates significant advantages in tracking accuracy, robustness, and engineering practicality.

References

[1] Y. Marani, E. Feron and M. -T. L. Kirati, "Observer-based Control of an Unmanned Aerial Vehicle in a Non-inertial Reference Frame," 2024 IEEE Conference on Control Technology and Applications (CCTA), Newcastle upon Tyne, United Kingdom, 2024, pp. 107-113.

[2] B. Zhang et al., "CoNi-MPC: Cooperative Non-inertial Frame Based Model Predictive Control," in IEEE Robotics and Automation Letters, vol. 8, no. 12, pp. 8082-8089, Dec. 2023.

[3] Velasco–Villa M, Rodriguez–Angeles A, Maruri–López IZ, Báez-Hernández JA, Cruz Morales RD (2024) Leader–follower formation control based on non-inertial frames for non–holonomic mobile robots. PLOS ONE 19(1): e0297061.

[4] Mu, L., Li, Q., Wang, B., Zhang, Y., Feng, N., Xue, X., & Sun, W. (2023). A Vision-Based Autonomous Landing Guidance Strategy for a Micro-UAV by the Modified Camera View. Drones, 7(6).

[5] C. Wang et al., "Integrated Learning-Based Framework for Autonomous Quadrotor UAV Landing on a Collaborative Moving UGV," in IEEE Transactions on Vehicular Technology, vol. 73, no. 11, pp. 16092-16107, Nov. 2024.

[6] Cheng, C., Li, X., Xie, L., & Li, L. (2023). A Unmanned Aerial Vehicle (UAV)/Unmanned Ground Vehicle (UGV) Dynamic Autonomous Docking Scheme in GPS-Denied Environments. Drones, 7(10).

[7] Huzaefa, F.; Liu, Y.C. Force distribution and estimation for cooperative transportation control on multiple unmanned ground vehicles. IEEE Trans. Cybern. 2021, 53, 1335–1347.

[8] P. Tokekar, J. V. Hook, D. Mulla, and V. Isler, "Sensor planning for a symbiotic UAV and UGV system for precision agriculture," IEEE Trans. Robot., vol. 32, no. 6, pp. 1498–1511, Dec. 2016.

[9] K. Dorling, J. Heinrichs, G. G. Messier, and S. Magierowski, "Vehicle routing problems for drone delivery," IEEE Trans. Syst., Man, Cybern. Syst., vol. 47, no. 1, pp. 70–85, Jan. 2017.

[10] Z. Xun et al., "CREPES: Cooperative RElative Pose Estimation System," 2023 IEEE/RSJ International Conference on Intelligent Robots and Systems (IROS), Detroit, MI, USA, 2023, pp. 5274-5281.

[11] Sui, Y., Yang, Z., Zhuo, H., You, Y., Que, W., & He, N. (2024). A Fuzzy Pure Pursuit for Autonomous UGVs Based on Model Predictive Control and Whole-Body Motion Control. Drones, 8(10), 554.

[12] P. Tyagi, Y. Kumar and P. B. Sujit, "NMPC-based UAV 3D Target Tracking In The Presence Of Obstacles and Visibility Constraints," 2021 International Conference on Unmanned Aircraft Systems (ICUAS), Athens, Greece, 2021, pp. 858-867.

[13] Munasinghe, I., Perera, A., & Deo, R. C. (2024). A Comprehensive Review of UAV-UGV Collaboration: Advancements and Challenges. Journal of Sensor and Actuator Networks, 13(6), 81.

[14] L. Quan, "Robust and efficient trajectory planning for formation flight in dense environments," IEEE Trans. Robot., pp. 1–20, 2023.

[15] Y. Li, G. Lu, D. He, and F. Zhang, "Rob centric model-based visual serving for quadrotor flights," IEEE/ASME Trans. Mechatronics, vol. 28, no. 4, pp. 2155–2166, Aug. 2023.

[16] de Castro, G.G.R.; Santos, T.M.B.; Andrade, F.A.A.; Lima, J.; Haddad, D.B.; Honório, L.d.M.; Pinto, M.F. Heterogeneous Multi-Robot Collaboration for Coverage Path Planning in Partially Known Dynamic Environments. Machines 2024, 12, 200.

[17] Ou, B.; Liu, F.; Niu, G. Distributed Localization for UAV–UGV Cooperative Systems Using Information Consensus Filter. Drones 2024, 8, 166.

[18] Aiello, G.; Hopps, F.; Santisi, D.; Venticinque, M. The Employment of Unmanned Aerial Vehicles for Analyzing and Mitigating Disaster Risks in Industrial Sites. IEEE Trans. Eng. Manag. 2020, 67, 519–530.

[19] Shakhatreh, H.; Sawalmeh, A.H.; Al-Fuqaha, A.; Dou, Z.; Almaita, E.; Khalil, I.; Othman, N.S.; Khreishah, A.; Guizani, M. Unmanned aerial vehicles (UAVs): A survey on civil applications and key research challenges. IEEE Access 2019, 7, 48572–48634.

[20] Zhang, J.; Yue, X.; Zhang, H.; Xiao, T. Optimal Unmanned Ground Vehicle-Unmanned Aerial Vehicle Formation-

Maintenance Control for Air-Ground Cooperation. Appl. Sci. 2022, 12, 3598.

[21] A. Romero, S. Sun, P. Foehn, and D. Scaramuzza, "Model predictive contouring control for time-optimal quadrotor flight," IEEE Trans. Robot., vol. 38, no. 6, pp. 3340–3356, Dec. 2022.

[22] Ahmed, F.; Jenihhin, M. A Survey on UAV Computing Platforms: A Hardware Reliability Perspective. Sensors 2022, 22, 6286.

[23] Chen, X.; Wu, Y.; Xu, S. Mission Planning of UAVs and UGV for Building Inspection in Rural Area. Algorithms 2024, 17, 177.

[24] Tang, H.; Chen, Y.; Ali, I. Cross-dimensional Distributed Control for Heterogeneous UAV-UGV Systems with Nonzero Leader Input. IEEE Trans. Intell. Veh. 2024. early access.

[25] Zhang, S.; Wang, H.; He, S.; Zhang, C.; Liu, J. An Autonomous Air-Ground Cooperative Field Surveillance System with Quadrotor UAV and Unmanned ATV Robots. In Proceedings of the 2018 IEEE 8th Annual International Conference on CYBER Technology in Automation, Control, and Intelligent Systems (CYBER), Tianjin, China, 19–23 July 2018.

[26] P. Sujit and D. Ghose, "Search using multiple uavs with flight time constraints," IEEE Transactions on Aerospace and Electronic Systems, vol. 40, no. 2, pp. 491–509, 2004.

[27] G. Morgenthal and N. Hallermann, "Quality assessment of unmanned aerial vehicle (uav) based visual inspection of structures," Advances in Structural Engineering, vol. 17, no. 3, pp. 289–302, 2014.